Author/s:
Ludescher, D;Wesemann, L;Schwab, J;Karst, J;Sulejman, SB;Ubl, M;Clarke, BO;Roberts, A;Giessen, H;Hentschel, M

Title:
Optical sieve for nanoplastic detection, sizing and counting

Date:
2025-10-01

Citation:
Ludescher, D., Wesemann, L., Schwab, J., Karst, J., Sulejman, S. B., Ubl, M., Clarke, B. O., Roberts, A., Giessen, H. & Hentschel, M. (2025). Optical sieve for nanoplastic detection, sizing and counting. Nature Photonics, 19 (10), pp.1138-1145. https://doi.org/10.1038/s41566-025-01733-x.

Published article in Nature Photonics, 19, 1138–1145 (2025)
https://www.nature.com/articles/s41566-025-01733-x

Optical Sieve for Nanoplastic Detection, Sizing, and Counting

D. Ludescher [1], L. Wesemann [2], J. Schwab [1], J. Karst [1], S. B. Sulejman [2], M. Ubl [1], B. O. Clarke [3], A. Roberts [2], H. Giessen [1], and M. Hentschel [1,*]

[1] *4th Physics Institute and Research Center SCoPE, University of Stuttgart, Pfaffenwaldring 57, 70569 Stuttgart, Germany*
[2] *ARC Center of Excellence for Transformative Meta-Optical Systems (TMOS), School of Physics, The University of Melbourne, Victoria 3010, Australia*
[3] *Australian Laboratory for Emerging Contaminants, School of Chemistry, University of Melbourne, Victoria 3010, Australia*
[*] *Corresponding author: Mario Hentschel (m.hentschel@pi4.uni-stuttgart.de)*

Abstract

Micro- and nanoplastic particles are ubiquitous environmental pollutants, threatening human health, aquatic, and soil ecosystems. These minute synthetic fragments, persisting for centuries, infiltrate the food chain, posing potential health risks through bioaccumulation in various tissues, toxicity, and exposure to associated chemicals. While macro- and microplastics are intensively examined in environmental and biological research, information about nanoplastics with diameters below 1 µm is limited. Such particles can cross biological borders, including the blood-brain barrier, posing a greater health risk than microplastics. Apart from the mere detection of such particles, gaining an understanding of size distribution, numbers, and size limits will be crucial in assessing their impact on global ecosystems and human health. Here, we establish an optical sieve that utilizes Mie void resonances for nanoplastic detection and sizing. The optical sieve consists of arrays of optically resonant voids with different diameters that simultaneously serve as filtering and sorting elements as well as all-optical reporters, requiring only an optical microscope and a standard camera with an RGB sensor in combination with colorimetric analysis. The system is evaluated using a synthesized real-world sample with a plastic particle mass concentration of 1.5 µg/ml. Our approach consequently delivers statistical information on numbers, size, and size distribution via the observation of distinct color changes, overcoming the need for advanced techniques such as scanning electron microscopy. The proposed method offers a straightforward, highly accessible, and mobile solution, making it an efficient and easily implemented tool for environmental and biological research.

Plastics, first introduced in the 1930s, have become a critical environmental challenge in the twentieth century due to their ubiquitous distribution, persistence, bioaccumulation, and increasing evidence of toxicity[1–3]. Plastic pollution was first reported in 1972, focusing solely on large plastic objects responsible for entangling marine mammals in fishing nets or plastic debris[4,5]. In 2004, researchers highlighted the environmental threat of microplastics, synthetic plastic particles smaller than 5 mm with a significant impact on human health[6–8]. These plastic particles are strongly redistributed across various ecosystems and can be found in even the most remote locations such as sea surfaces and sediments[9–13], streams and rivers[14–16], in the groundwater[17], in the atmosphere[18,19], and on mountains[20,21]. Their pervasiveness extends to human tissues, including blood[22], the placenta[23], and vital organs such as the lungs, liver, and kidneys[24,25], as well as to food and drinks[26–29].

Microplastics, however, are not the final stage of plastic degradation[30]. Over time, they break down further due to UV radiation, biodegradation, mechanical stress, or thermal degradation into particles smaller than 1 µm, termed nanoplastics[7]. These particles are even more concerning than microplastics due to their size and their potential to penetrate biological borders such as the epidermal, blood-brain, blood-air, or placental barrier[31–33]. Humans are exposed via ingestion, inhalation, or dermal exposure and when internalized, the particles can accumu-late in vital organs and the vascular system, potentially causing severe health effects[34]. In addition, nanoplastics are known to absorb toxic substances, such as persistent organic pollutants or heavy metals, which may dissolve into the body upon ingestion[2,35,36].

While the harmful characteristics of nanoplastics are widely acknowledged, substantial knowledge gaps remain[37]. The reason mainly lies in the challenge of nanoplastic detection. Due to the small sizes, advanced separation and filtration techniques followed by complex characterization techniques such as scanning electron microscopy are required[38–40]. As a consequence, there is little to no available data on actual environmental let alone biological samples. To overcome this experimental challenge, the common theme in state-of-the-art environmental nanoplastic studies is the usage of synthesized nanospheres as a proxy[31,41–43].

In the field of photonic sensing, various strategies have been explored, including dielectric nanostructures[44–49], plasmonic systems[50–52], and bound states in the continuum[53–56]. In comparison to these concepts, our approach leverages the concept of Mie void resonances[57]. The resonators are open cylindrical hole cavities in the surface of a high refractive index material such as gallium arsenide or silicon. Light can be trapped and resonate at distinct wavelengths, depending on the geometry, size, and refractive index. Here, the Mie voids of our optical sieve serve a dual function: the void-resonators of varying size sort and filter the particles - like a classical sieve - while simultaneously reporting this information all-optically due to their localized light modes. This approach offers remarkable simplicity and, unlike other well-established and powerful techniques in nanoplastic research such as dynamic light scattering (DLS), requires no additional and complex instrumentation as only an optical microscope is needed[58,59].

In this work, we introduce this novel strategy to detect nanoplastics with sizes down to a few hundred nanometers. The color change upon particle capture can be used to detect, size, and count nanoplastic particles. A standard optical microscope allows for the observation of the resonant scattering spectrum of the Mie void by simple colorimetric analysis. The detectable shift in resonance wavelength thus delivers statistical information about the nanoplastic sample. In accordance with standard procedures in the literature, we demonstrate the functionality and validity of our concept utilizing samples of known composition based on commercial polystyrene spheres. This approach is remarkably simple and fast, requiring only an optical microscope without the need for complex measurement devices.

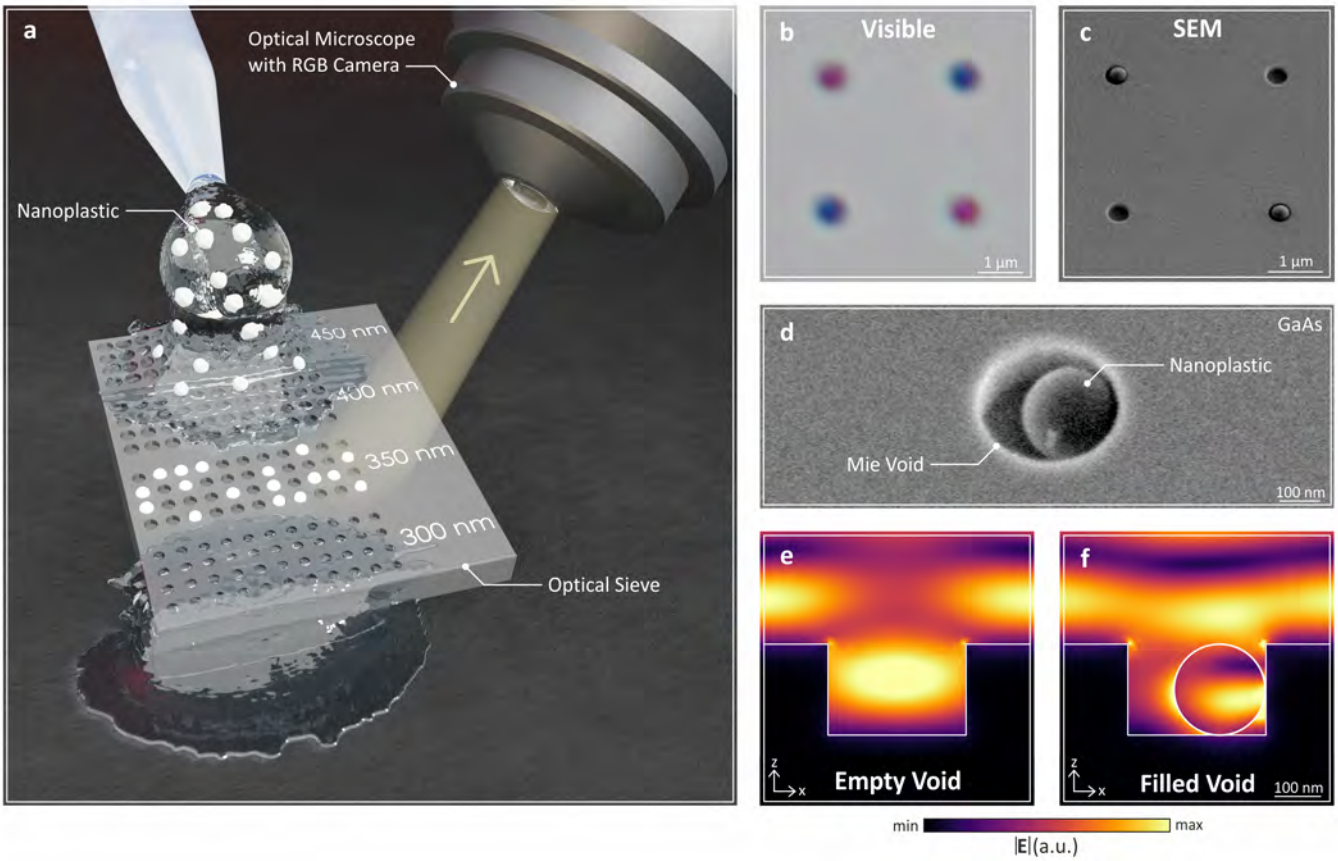

Figure 1: Nanoplastic detection utilizing the optical sieve. **a**, The general detection principle is presented, showing the deposition of nanoplastic samples onto an optical sieve to identify plastic particles. The optical sieve consists of arrays of voids with different diameters, serving the dual function of sorting the particles according to their size and reporting the presence of particles in voids all-optically due to the localized light modes. Particles matching the void size fall into the corresponding holes, remaining trapped after the sieve is cleaned, while voids of mismatched sizes remain mostly empty. An RGB camera attached to a microscope (indicated in the upper right) evaluates the optical sieve in reflection geometry. The illumination assembly was omitted for clarity. A color shift indicates the presence of plastic particles in the voids. **b** and **c**, Microscope and SEM image display a partially filled sample with 2x2 voids. Filled voids (top left and bottom right) appear red in contrast to empty voids (blue). The SEM image confirms this observation. **d**, A single filled void containing a 200 nm nanoplastic particle is shown. The voids, dry etched into GaAs, have a diameter of 350 nm. **e** and **f**, Simulations of the electric field for empty and filled voids are presented at the bottom. The incident wavelength of the light is 380 nm.

The ultimate goal of our work is the creation of a nanoplastic test strip that permits to obtain statistical data all-optically on the size, size distribution, and concentration of nanoplastic particles in real-world samples. To this end, we first establish the working principle by presenting sizing and counting of pure plastic samples, followed by demonstrating our method on a synthesized sample based on a real-world matrix composed of lake water, sand, and a distribution of different nanoplastic particles.

Nanoplastic detection using Mie void resonances

In Fig. 1a, the general working principle of the optical sieve is illustrated. It comprises arrays of voids in the otherwise flat surface of a high refractive index material with diameters that increase progressively from the bottom to the top. A liquid solution containing nanoplastic particles is flushed over the sieve. By tailoring the diameters and depths of the voids, nanoplastic spheres with matching dimensions are trapped with an increased probability within the voids due to van der Waals (vdW) forces. Subsequently, the optical sieve is cleaned multiple times with water.

If the voids are too small, particles either do not enter the voids at all or rest on top of these, allowing for easy removal in a successive cleaning process with water and ultrasonication. Conversely, if the voids are too large, the particles fall into the voids but experience insufficient adhesive forces, making them removable during cleaning. Consequently, only voids with matching diameters and depths retain particles while mismatched cavities remain mostly empty. The greater the mismatch between the void dimensions and the particle sizes, the lower is the probability of particles remaining in the voids. The influence of the geometric match between the voids and the deposited particles will be investigated in more detail during sizing and counting experiments of nanoplastic particles. Note that particles trapped in voids with closely matching diameters cannot be removed by the cleaning process, as the present vdW forces are sufficiently strong to retain the particles.

We highlight that the term optical sieve does not imply that the sieving process is driven optically by light. Instead, the concept utilizes Mie voids to filter nanoplastic particles from a liquid solution and to separate smaller particles from larger particles, with *optical detection* by detuning the Mie void resonance upon particle capture. Light is trapped inside the void, forming a standing wave mode that resonates with a wavelength determined by the diameter and depth of the void. Upon a change in the refractive index inside the cavity when a nanoplastic particle is trapped, this resonant wavelength shifts and produces a color change. Combining a microscope with an RGB camera allows us to observe the color differences between empty and filled voids and enables colorimetric analysis.

In Fig. 1b and 1c, a light microscope and SEM image depict a 2x2 array of voids. The microscope image reveals empty voids (upper right and lower left) with a blue appearance, while the filled voids exhibit a red color. The imaging setup is presented in Fig. SI 1. This observation is confirmed by the SEM image.

Fig. 1d presents an SEM image of a single void, approximately 350 nm in diameter, which contains a 200 nm nanoplastic particle resting on the bottom of the void. This SEM image serves as the template for full-wave simulations of the electric field distribution displayed in Fig. 1e and 1f. Cross-sections of the x-z-plane are plotted for an empty void (Fig. 1e) and a filled void (Fig. 1f) at an incident light wavelength of 380 nm. The simulated results reveal strong light confinement of the modal volume within the air void, with minimal leakage into the host material. In the case of a filled void, the nanoplastic particle interacts strongly with the localized mode, resulting in a resonance wavelength shift.

In addition to Fig. 1, the detection method is not limited to particles with a specific diameter of 350 nm. Fig. 2 demonstrates the detection capability of our Mie void sample for nanoplastic particles with diameters of 200 nm, 350 nm, 465 nm, 550 nm, and 1 µm (from top to bottom). For each particle diameter, 3x3 arrays of voids are depicted using SEM (left) and microscope images (right). Particles with a diameter of 200 nm represent the approximate lower detection limit achievable using a standard optical microscope. Detecting smaller particles would require smaller and shallower voids, resulting in a resonance shift of the empty voids towards shorter

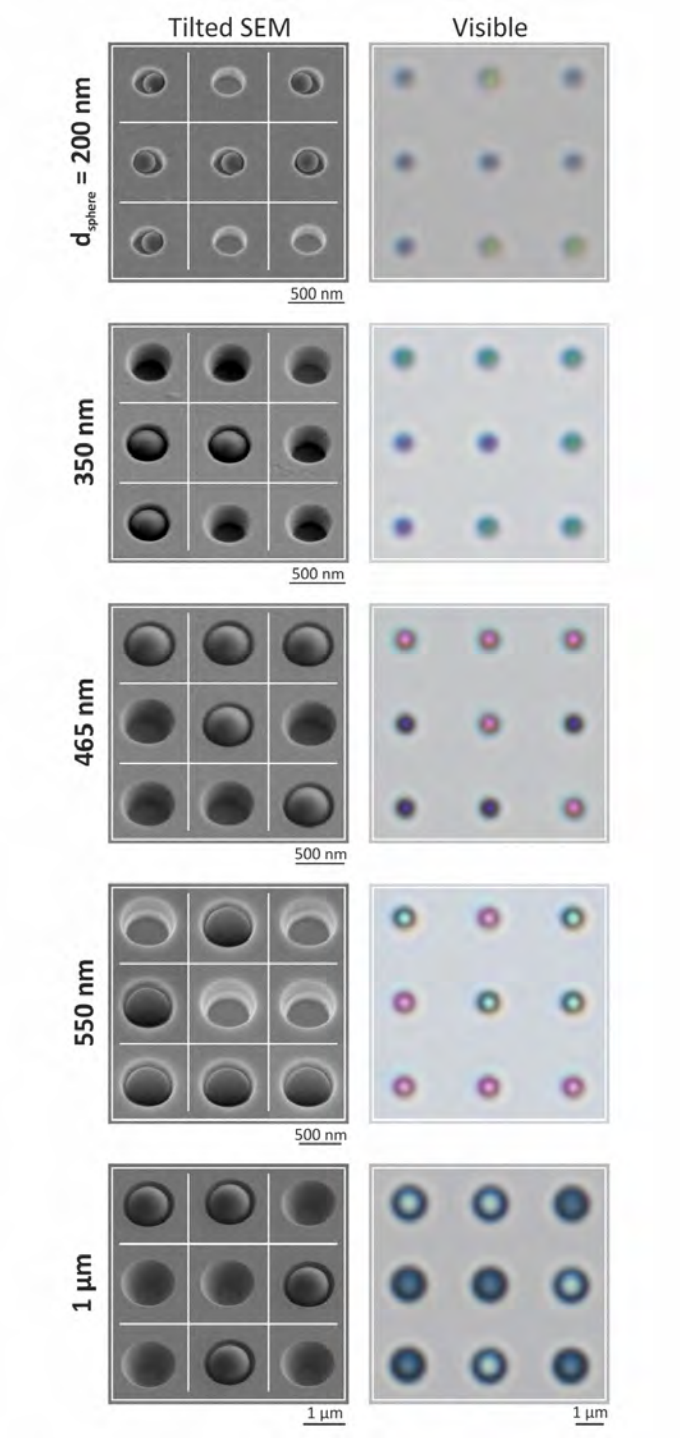

Figure 2: Color change induced by single plastic particles. The color change caused by filling voids with single nanoplastic spheres with different diameters is shown (200 nm, 350 nm, 465 nm, 550 nm, and 1 µm,). On the left, tilted SEM close-ups of each 3x3 array are shown. On the right, microscope images display the color shift in these arrays. The SEM images focus on each void, omitting the blank space.

wavelengths in the UV spectral range.
A distinct color change is evident in the microscope images, enabling the detection of nanoplastic particles for all five particle sizes. The void diameter is always slightly bigger than the particle diameter. Simulated field distributions for all five particle diameters are shown in Fig.

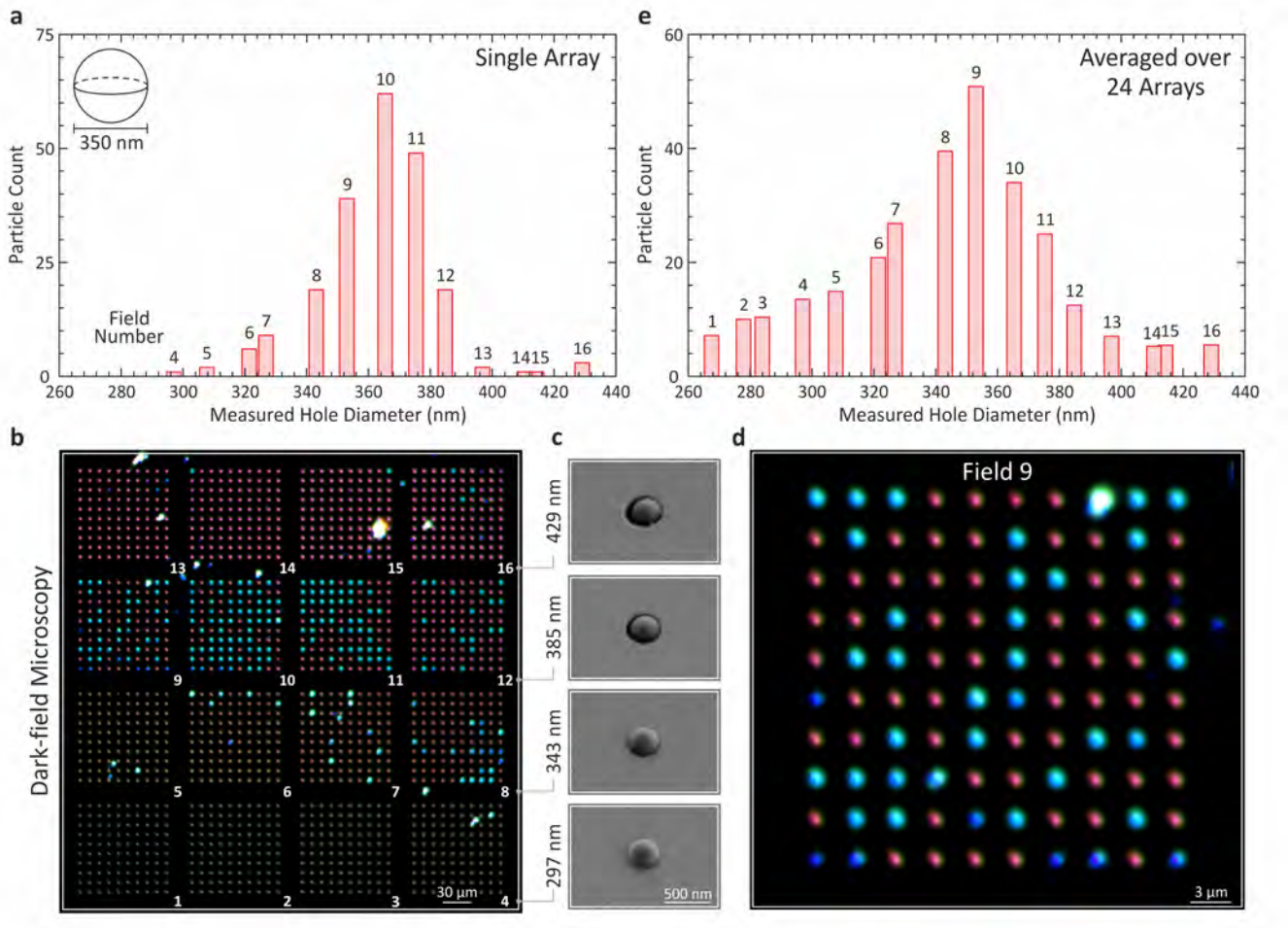

Figure 3: Nanoplastic particle sizing. Nanoplastic spheres (350 nm diameter) are deposited onto a sizing sample. **a**, The histogram displays the occupancy data of a single sizing sample with 16 fields, each containing 10x10 Mie voids. Void diameters increase from 267 nm (field 1) to 429 nm (field 16), with fields 9 to 11 showing the highest occupancy, aligning with void sizes in the range of 350 nm. **b**, A darkfield image of the analyzed sizing sample reveals bright blue spots, indicating filled Mie voids. Fields are numbered starting at the bottom left to the upper right. **c**, The central SEM images show individual voids from fields 4 (297 nm), 8 (343 nm), 12 (385 nm), and 16 (429 nm) with a trapped plastic particle, illustrating how spheres begin to settle deeper as void sizes increase. **d**, A close-up of field 9 shows filled voids with varying shades of blue, reflecting differences in particle depth within the voids. Bright blue denotes particles deep within the voids, while dark blue indicates particles on top of the voids. **e**, A histogram averaging 24 sizing samples shows peak occupation in field 9 with a void size of 353 nm, closely matching the sphere diameter.

SI 2. In addition, the spectral shift between empty and filled voids for particles with diameters of 550 nm and 1 µm was measured using a microspectroscopy setup (Fig. SI 3)[60].

Sizing and counting of nanoplastic particles

Thus far, we have demonstrated the ability to detect nanoplastic particles of varying diameters from a pure liquid suspension. To further explore the analytical potential of this method, we investigated whether additional information about the particles, such as the size and the number of particles in a larger void can be obtained through careful sample analysis using the

associated color changes.
Fig. 3 illustrates the principle of sizing nanoplastic particles with a nominal diameter of 350 nm. The histogram depicted in Fig. 3a is generated from a single detection array consisting of 4x4 fields with increasing void diameters. The corresponding dark-field image of the sizing sample is presented in Fig. 3b. The sizing sample includes 16 fields, each field containing 10x10 voids. The void diameter and depth increase from about 267 nm and 250 nm in field 1 (bottom left) to 429 nm and 320 nm in field 16 (top right). The field numbers are labeled in the dark-field image, where filled voids appear as blue spots while empty voids are reddish. The histogram in Fig. 3a exhibits distinct peaks for fields 9 to 11, corresponding to void diameters between 353 nm and 375 nm. These values are in close agreement with the expected particle diameter of 350 nm.
Fig. 3c presents SEM images of single voids filled with a particle in fields 4 (297 nm void diameter), 8 (343 nm), 12 (385 nm), and 16 (429 nm). For smaller void diameters, the particles rest only at the void rim, resulting in reduced vdW interaction and easier removal during subsequent rinsing. As the void diameter increases, the particles start to settle deeper into the voids, touching the walls as well as the bottom of the void. However, for very large voids (fields 13 and onwards), the particles lose contact with the void walls while still resting on the bottom of the void. A close-up of field 9 with a void diameter of 353 nm is shown in Fig. 3d. This field exhibits high occupation numbers with 39 filled voids (blue). In this sizing experiment, deviations in z-position of the particles do not introduce additional measurement complexity, as the analysis is limited to distinguish filled from empty voids. However, in more complex measurements involving smaller refractive index contrasts, the z-position variation can influence the optical response and must be taken into account.
Fig. 3e presents an averaged histogram, summarizing occupation numbers across 24 individual sizing samples. Unlike Fig. 3a, which focuses on a single sizing sample, this histogram provides broader statistical insight. In agreement with Fig. 3a, the highest averaged occupation is observed in fields 8 to 10, corresponding to void diameters between 343 nm and 365 nm. We attribute the broader occupancy distribution in Fig. 3e to slight variations in the void sizes between samples and deviations in particle sizes from the nominal value. This figure illustrates the probabilistic nature of the trapping process. As the diameter of the voids matches that of the particles more closely, the number of particles retained after the cleaning process increases accordingly. A size mismatch between void and particles does not prevent trapping entirely but reduces the probability, resulting in fewer particles remaining within the voids.
As real-world nanoplastic samples can have a wide distribution of sizes and our Mie-void optical sieve features an entire range of hole diameters and depths, it is quite likely that very small nanoparticles can agglomerate inside a larger hole and combine into groups of two or three particles. Therefore, we investigated whether that particle number in a single void can be determined as well through colorimetric analysis. As the observable void color is sensitive to refractive index changes, the number of particles within the void has a direct influence on the color. With a fixed void geometry, the resonance shift arises solely from changes in the effective refractive index due to different particle numbers.
To test this effect, a mixture of 350 nm and 550 nm particles is deposited to count the number of particles inside a single void. Here, the voids have a diameter of 830 nm and a depth of 550 nm to accommodate multiple particles. Fig. 4a presents a microscope image of a counting sample that comprises 9x9 fields, each field containing a 3x3 array of voids. A magnified view on one specific field is depicted in Fig. 4b with the corresponding SEM image in Fig. 4c. In the magnified optical image, five different colors are visible. Empty voids appear blue, while filled voids display increasingly reddish hues as the number of particles within the void

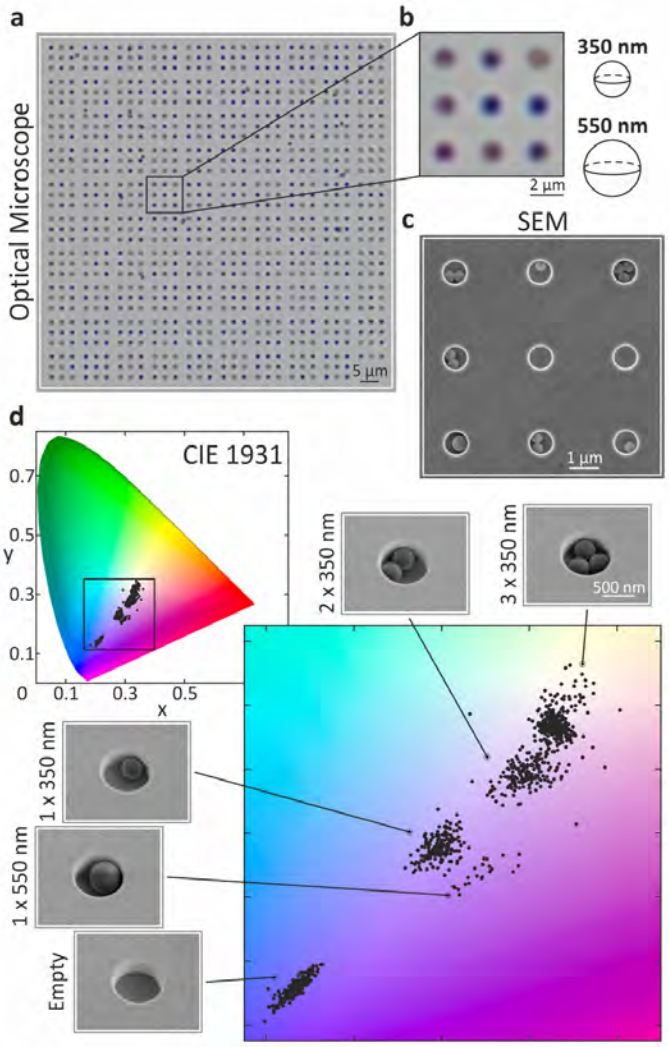

Figure 4: Colorimetric analysis for nanoparticle counting. The color change of voids in the presence of spheres can be used to count the number of spheres. Here, spheres with diameters of 350 nm and 550 nm are deposited onto the sample. **a**, an optical microscope image and **b**, a zoom-in can be seen indicating the five different colors created by the varying void occupation numbers. In **c**, the corresponding SEM image of the zoom-in can be found. All five states (empty, one, two, three 350 nm spheres, and one 550 nm sphere) are present in this 3x3 field. **d**, colorimetric analysis of the full optical microscope image is presented in the CIE 1931-diagram. In the zoom-in on the bottom right five separated clusters according to the different cases can be identified. SEM images of single, occupied voids for the five different states can be found surrounding the diagram.

increases. The SEM image verifies the presence of all five states, i.e., empty voids, voids containing one, two, or three 350 nm particles, and voids filled with one 550 nm sphere, with each particle configuration occupying a distinct volume within the fabricated voids.
To quantify these observations, a color readout code was applied to identify the color of each void on the counting sample. Consequently, the analysis can be applied to all 729 voids in the sample. To this end, the code locates each void in a standard optical microscope image and reads out the observed color. The colorimetric data can then be plotted on a CIE 1931-diagram as displayed in Fig. 4d. A closer inspection of the zoom-in of the CIE diagram reveals five separate clusters, each corresponding to one of the five particle states. Around

this image, SEM images of individual, filled voids illustrate the specific particle arrangement associated with each color cluster. For each particle state, the data points forming a cluster cover a specific region in the CIE 1931-diagram. In addition to fabrication-related variations in void geometry, and differences in particle size and position, imperfect illumination in the microscope setup further contributes to the apparent slight color differences. Further details on the color readout are provided in the methods section. The simulated capability to detect different materials based on their different refractive indices is illustrated in Fig. SI 4.

Optical sieve used for synthesized real-world samples

Unfortunately, readily available real-world samples containing nanoplastic particles are to the best of our knowledge, not yet available due to the required demanding filter techniques. Additionally, the validation of a technique requires knowledge about the sample in order to confirm the obtained findings. In order to address these issues, we synthesized a sample in accordance with standard procedures reported in literature[8,31,37,61].

Fig. 5a shows an SEM image of the deposited synthesized sample, revealing a mixture of sand, debris, and nanoplastic particles before the sample is cleaned. The composition of this mixture is described in Fig. 5b: lake water from a university lake was mixed with clean sand and nanoplastic particles of 350 nm, 550 nm, and 1 µm diameter. To mimic real-world conditions, unfiltered and untreated lake water was used as the liquid medium to ensure the presence of biological material. Compared to methods like DLS which is not capable of distinguishing between plastic and organic material, our system eliminates the need to pre-clean biological material from the liquid environment, simplifying nanoplastic detection. The exact composition is given in the methods section, and Fig. SI 5a, 5b, and 5c depict the collection site of the lake water, the synthesized real-world sample, and the deposition on the optical sieve, respectively.

The synthesized sample has been deposited on the optical sieve. After drying, the sample is rinsed with water. During this cleaning process, large contaminants such as larger sand particles are easily removed using coarse filters, while smaller debris in the size range of the nanoplastic particles require more careful and thorough cleaning. Selected dark-field images of the optical sieve are shown in Fig. 5c, with void diameters increasing from 300 nm (top) to 1120 nm (bottom). Here, the void depth increases from 230 nm (top) to about 330 nm (bottom). Odd rows remain mostly empty, while the depicted even rows display high occupation numbers. Bright spots in the dark-field images of the optical sieve indicate filled voids. Notably, voids with diameters of 355 nm, 540 nm, and 985 nm correspond to high occupation numbers, aligning well with the diameters of the added particles.

Fig. 5d presents magnified images of the microscope pictures for voids with diameters of 355 nm (pink), 540 nm (orange), and 985 nm (blue), alongside corresponding SEM images. The SEM images, obtained from areas indicated by the white squares, verify the observation. Organic material present in the sample results in a rough surface on the host material visible in the SEM images, however, most of the dirt and larger sand debris is effectively removed from the optical sieve during cleaning.

To compare the occupation numbers across detection arrays, a histogram is shown in Fig. 5e. The full optical sieve, consisting of 30 detection arrays with increasing void diameters is depicted in Fig. SI 6. The histogram reveals three distinct peaks, corresponding to fields with void diameters matching the diameters of the mixed-in nanoparticles.

Note that some voids are incorrectly filled with debris or mismatched spheres. This issue arises from residual organic material and insufficient cleaning, which can trap smaller spheres

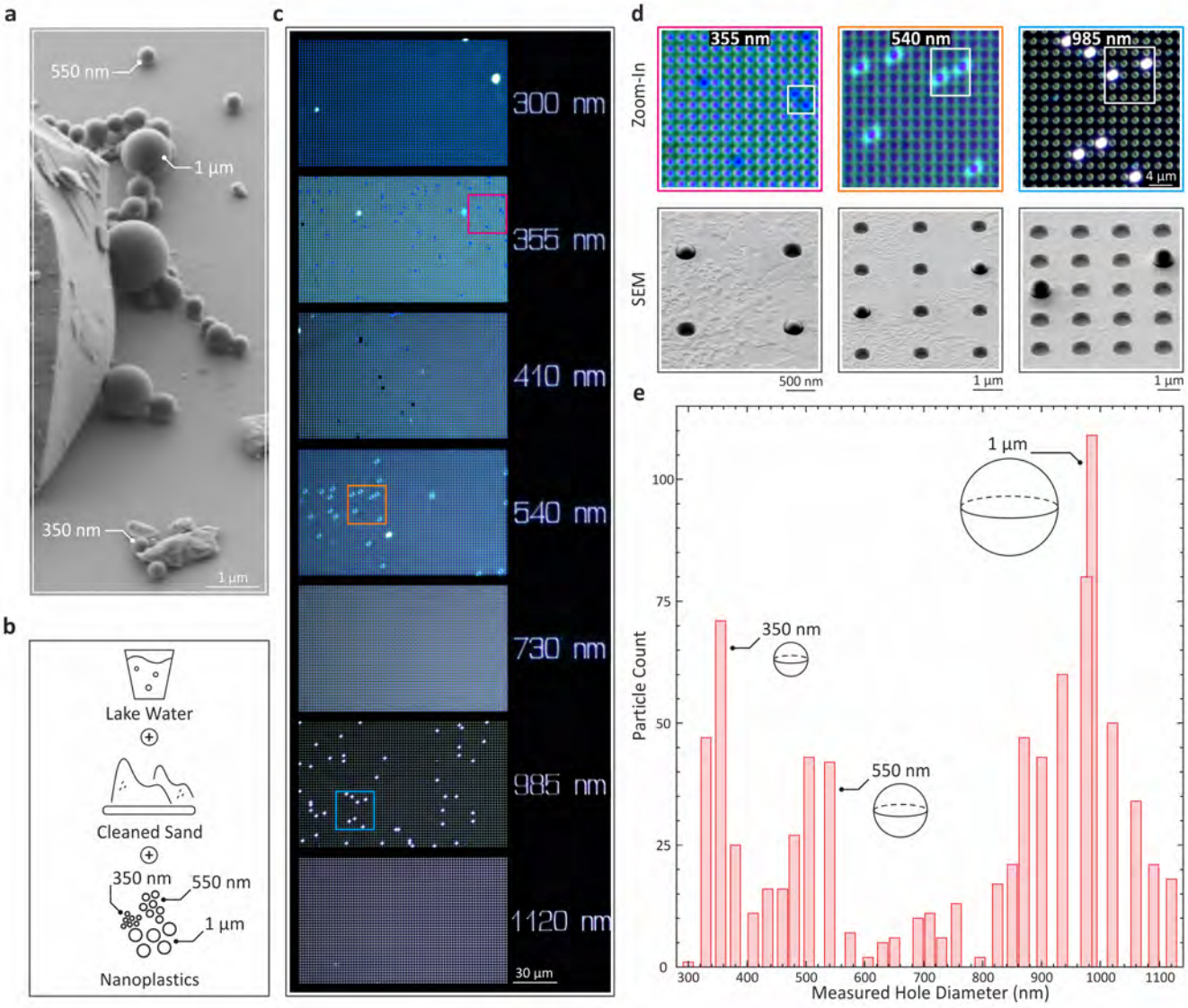

Figure 5: Detecting nanoplastic particles in synthesized real-world samples. **a**, An SEM image of the synthesized sample displays a mixture of dirt, various particles, and nanoplastic spheres with diameters of 350 nm, 550 nm, and 1 µm, before the sample is cleaned. **b**, The sample composition includes lake water, cleaned sand, and added particles, which are mixed and deposited on the optical sieve. **c**, Selected dark-field microscope images of the complete optical sieve are presented. The full test strip consists of 30 individual detection arrays. The void diameter ranges from 300 nm (top) to 1120 nm (bottom). **d**, Zoom-ins highlight the color change between filled and empty voids, confirmed with SEM images of the according areas. Arrays with void diameters of 355 nm (pink), 540 nm (orange), and 985 nm (blue) exhibit higher filling rates. **e**, The histogram displays the occupancy rates for each of the 30 detection arrays, with distinct peaks corresponding to the bead sizes.

in voids that are too large. However, these voids can easily be distinguished from correctly filled voids or empty voids through colorimetric analysis. Due to the substantial refractive index contrast between the debris and the polymer material, correctly filled voids can be distinguished from the incorrectly filled ones based on their color response. A detailed analysis of the incorrectly filled voids is presented in Fig. SI 7. It should be noted that plastic particles in real environmental samples typically exhibit irregular, non-spherical shapes. For

such particles, a general reduction in trapping efficiency is expected. However, if adhesion forces are sufficiently strong, these particles may still be retained in voids larger than their smallest dimension.
The working principle of the displayed optical sieve is verified in Fig. SI 8. Here, a reduced optical sieve formed by 11 detection arrays, is used to examine a controlled sample in which nanoplastic particles are mixed with clean water and deposited on the optical sieve. Similar results are obtained for the reduced optical sieve. The long-term stability and robustness of the optical sieve are investigated in Fig. SI 9 by comparing initial SEM images with those acquired eight months later. For this measurement, a plastic particle concentration of approximately 1.5 µg/ml in lake water was utilized.

Conclusion

We present a novel approach for nanoplastic detection utilizing Mie void resonances in an optical sieve. Our method enables the detection of nanoplastic particles with diameters as small as 200 nm, effectively covering the important size range for nanoplastics. The general principle is based on a resonance shift of the localized Mie mode confined in air voids, induced by an effective refractive index change. This technique requires only a standard optical microscope and, when combined with colorimetric analysis, offers a straightforward detection method.
Beyond detection, we demonstrate the ability to size and count nanoplastic particles within a single void by analyzing the color change. Plotting the obtained colors in a CIE diagram reveals distinct color clusters corresponding to different particle numbers. Furthermore, we extend the application of this approach to synthesized real-world samples containing mixed-in nanoparticles, showcasing the potential for environmental analysis.
This platform provides a powerful tool for nanoplastic detection and offers opportunities for further improvements. Not only is the detection of plastic particles important, but gaining information about the material properties is also relevant. The void color itself is inherently sensitive to refractive index variations, making the system capable of distinguishing between materials with different refractive indices. In combination with more complex analysis methods such as µ-FTIR, µm-Raman spectroscopy, and microscopic stimulated Raman microscopy, detailed information about material properties can be extracted as the particles are directly trapped within the voids[62,63]. Future work could involve the investigation of non-spherical particles to gain deeper insights into the trapping mechanisms and testing real environmental samples to further validate the functionality of the optical sieve. Certainly, machine-learning and AI methods can help in identifying and quantifying nanoplastic samples under real-world conditions, discriminating non-plastic materials as well as larger debris. This could render our method even more accurate. This way, nanoplastics in blood, in tissue, and in other environmental and biological samples could be detected, sized, and counted in the future. Ultimately, we envision this method facilitating simple nanoplastic detection in test strips and mobile devices for a variety of scenarios.

Methods

Mie Void Sample Generation

In contrast to previous studies, the Mie voids in this work are fabricated using efficient dry etching processes in gallium arsenide (GaAs) instead of the more complex and time-consuming focused ion beam (FIB) milling[57]. The combination of electron-beam lithography and dry etching into GaAs significantly simplifies the sample fabrication process and greatly reduces the overall production time. As a result, the rapid and straightforward fabrication of samples enables cost-effective single-use test strips. The process begins by spin-coating an electron-beam resist (AR-P 6200.13, 400 nm) onto a pre-cleaned GaAs substrate, serving as the etch mask. The spin-coating process involves a two-step routine: 2000 RPM for 5 s, followed by 4000 RPM for 55 s. The substrate is subsequently soft-baked on a hot plate at 180 °C for 3 minutes to stabilize the resist layer.

Electron-beam lithography (EBL) is performed on a commercial system (VOYAGER, Raith GmbH) with the following parameters: 50 kV acceleration voltage, 60 µm aperture, and 10 nm step size. A dose of 200 $\mu C/cm^2$ is applied to achieve high-resolution patterning.

After exposure, the resist is developed in AR 600-546 for 90 s, followed by immersion in AR 600-60 stopper solution for 30 s. Dry etching is carried out using an inductively coupled plasma (ICP) system (Oxford Instruments Plasmalab System 100) with $SiCl_4$ gas. The etching parameters are: 60 W RF power, 350 W ICP power, 6 sccm $SiCl_4$ flow rate, 5 sccm helium flow rate, and a chamber temperature of 30 °C. These settings result in an etching rate of 12.6 nm/s over large areas. Etching durations range from 25 s to 55 s, adjusted to control the void depth according to the required void sizes.

Upon completion of etching, the resist mask is removed by briefly immersing the sample in N-Ethylpentedrone (NEP) to ensure clean mask removal. Finally, the sample is rinsed with acetone and isopropyl alcohol (IPA) to eliminate any residual contaminants, completing the fabrication process.

Nanoplastic Samples

Nanoplastic particles with varying diameters (200 nm, 350 nm, 465 nm, 550 nm, and 1 µm) are deposited onto Mie void samples in the described experiments. These polystyrene beads, purchased from Polysciences, Inc., are supplied in aqueous solution. A detailed list of the nanoplastic particles used can be found in the Supporting Information (Fig. SI 10).

Prior to deposition, Mie void samples undergo oxygen plasma cleaning to enhance the surface hydrophilicity. To prevent particle accumulation, the nanoplastic solutions are subjected to strong ultrasonication in a water bath.

The prepared nanoplastic suspensions are then carefully deposited onto the Mie void samples. After allowing the water to evaporate completely, any residual particles are removed by immersing the sample in water, accompanied by ultrasonication. The cleaning process was conducted for 2 minutes at an ultrasonication frequency of 35 kHz with varying applied voltages between 100 V and 260 V depending on the complexity of the deposited sample matrix.

Imaging and Scanning Electron Microscopy

Optical images of empty and filled voids are captured both in bright-field and dark-field modes using a Nikon Eclipse LV100NM microscope. Depending on the array size, objectives with magnifications of 10x (NA 0.3), 20x (NA 0.45), and 50x (NA 0.8) are used. To reduce the effective numerical aperture, the A-stop is fully closed. To ensure color accuracy and to obtain reliable, comparable microscope images, white balance calibration was performed on the clean,

blank substrate prior to each camera capture. Illumination is provided by a Nikon Halogen lamp (LV-LH50PC), and images are recorded using the NIS Elements D software paired with a CCD camera. The results of bright-field and dark-field imaging are compared in Fig. SI 11. Scanning electron microscopy (SEM) images of most samples are obtained using a Hitachi S-4800 SEM. For the synthesized real-world sample, SEM imaging is performed on a Zeiss GeminiSEM560. All images are captured using a 30 ° observation angle.

Simulations

The numerical simulations of empty and nanoplastic-filled voids (PS and PMMA) (electric field distribution shown in Fig. 1 and Fig. SI 2 and the simulated reflectance spectra presented in Fig. SI 4) were performed using the finite-element method frequency-domain solver in COMSOL Multiphysics. The voids are modeled as conical holes in a gallium arsenide substrate, with air (refractive index of 1) assumed inside the voids and above the substrate. The dimensions of the holes are estimated from SEM images of fabricated samples. For simulations involving nanoplastic particles, spherical particles are positioned within the voids at locations corresponding to those observed in SEM images. The refractive indices of gallium arsenide and polystyrene are taken from the respective literature sources[64,65].

To mimic an infinite extension along the z-axis, perfectly matched layers (PMLs) were applied at the top and bottom boundaries of the simulation domain. Laterally, the system is treated as periodic, with a period of 900 nm for spheres with diameters of 200 nm, 350 nm, 465 nm, and 550 nm, and 1.2 µm for spheres with a diameter of 1 µm. Periodic boundary conditions were implemented to account for this periodicity. Excitation is introduced through a periodic port positioned in the air domain above the voids, generating a plane wave propagating in negative z-direction with x-oriented polarization.

Synthesized Real-World Sample

A synthetic probe was developed to mimic nanoplastics in environmental conditions. Lake water was collected from a local lake close to the University of Stuttgart (Collection site displayed in Fig. SI 5a) and used without prior filtration. Sea sand (Carl Roth GmbH + Co KG., cleaned with acid and annealed) was added, containing particles with diameters between 100 µm and 315 µm. In addition, nanoplastic particles in three distinct sizes were introduced into the mixture (350 nm, 550 nm, and 1 µm).

The final preparation consisted of 1 ml lake water, 0.57 g sand, and 2.5 µl of each nanoplastic particle size. In total, approximately 2.6 x 10^9 (350 nm), 9.1 x 10^8 (550 nm), and 1.1 x 10^8 (1 µm) particles are present in the composition, corresponding to a total concentration of 1.5 µg/ml by weight. When compared to other established detection techniques such as pyrolysis-gas chromatography-mass spectrometry (0.01 to 0.5 µg/ml)[66,67], or fluorescence, X-ray, or NMR spectroscopy (0.2 to 10 µg/ml)[68], our approach falls within a comparable range. The components were combined in a microcentrifuge tube and mixed by shaking and ultrasonication in a water bath (Fig. SI 5b).

The synthesized sample was then deposited and dried following the methods previously described. An image of the sample post-deposition and before cleaning is provided in Fig. SI 5c. After drying, sand and residual contaminants were removed by rinsing with water and using ultrasonication.

Code for Color Readout

The differentiation between empty and filled Mie voids is achieved through a MATLAB script designed to extract RGB values from specific pixels in an input image. By plotting these values

for example in a CIE color space diagram, it becomes straightforward to distinguish between filled and empty voids. This approach was applied to illustrate the nanoplastic counting capabilities within Mie voids (Fig. 4), as well as to quantify filled versus empty voids for sizing experiments (Fig. 3) and the synthesized real-world sample (Fig. 5). The CIE diagram effectively highlights the color differences, enabling a precise count of filled voids based on their color. The accuracy of the MATLAB code was validated by comparing its results with manually counted void occupation numbers.
The code starts by identifying all individual voids. A Fourier filter is applied, with parameters adjusted to detect voids irrespective of their fill state while excluding larger debris or dirt particles. Voids are identified based on the color contrast with the surrounding substrate. Once all voids are located, the user specifies the void radius in pixels and the MATLAB code reads and averages the color across the defined void area. Each void color is recorded as an RGB value, corresponding to its red, green, and blue channels. These RGB values can then be converted for plotting in a CIE diagram. This facilitates a clear distinction between filled and empty voids allowing for reliable and automated void counting.

Acknowledgments

The authors acknowledge a grant through the Australia-Germany Joint Research Cooperation Scheme (UA-DAAD, Deutscher Akademische Austauschdienst e.V. (Programm des Projektbezogenen Personenaustauschs Australien 2023 – 2025, 57654632)), Ministerium für Wissenschaft, Forschung und Kunst Baden-Württemberg (RiSC, Innovation Campus Future Mobility: Sd Manu1, Lab7), Vector Stiftung (MINT Innovations), European Research Council (Advanced Grant Complex-plas, PoC Grant 3DPrintedOptics), Deutsche Forschungsgemeinschaft (DFG, German Research Foundation) (SPP1839 Tailored Disorder, 431314977/GRK2642), and University of Stuttgart (Terra Incognita).
L.W., S.B.S., and A.R. acknowledge the Australian Government through the Australian Research Council Centre of Excellence Grant (CE200100010). S.B.S. acknowledges the support of the Ernst and Grace Matthaei Scholarship and the Australian Government Research Training Program Scholarship.

References

1. Nanoplastic should be better understood. *Nat. Nanotechnol.* **14,** 299 (2019).
2. Andrady, A. L. The plastic in microplastics: A review. *Mar. Pollut. Bull.* **119,** 12–22 (2017).
3. Fusco, L. *et al.* Nanoplastics: Immune Impact, Detection, and Internalization after Human Blood Exposure by Single-Cell Mass Cytometry. *Adv. Mater.,* 2413413 (2024).
4. Carpenter, E. J. & Smith Jr., K. L. Plastics on the Sargasso Sea Surface. *Science* **175,** 1240–1241 (1972).
5. Carpenter, E. J., Anderson, S. J., Harvey, G. R., Miklas, H. P. & Peck, B. B. Polystyrene Spherules in Coastal Waters. *Science* **178,** 749–750 (1972).
6. Thompson, R. C. *et al.* Lost at Sea: Where Is All the Plastic? *Science* **304,** 838–838 (2004).
7. Hartmann, N. B. *et al.* Are We Speaking the Same Language? Recommendations for a Definition and Categorization Framework for Plastic Debris. *Environ. Sci. Technol.* **53,** 1039–1047 (2019).

8. Thompson, R. C. *et al.* Twenty years of microplastic pollution research - what have we learned? *Science* **386,** 395 (2024).
9. Chubarenko, I. & Stepanova, N. Microplastics in sea coastal zone: Lessons learned from the Baltic amber. *Environ. Pollut.* **224,** 243–254 (2017).
10. Russell, M. & Webster, L. Microplastics in sea surface waters around Scotland. *Mar. Pollut. Bull.* **166,** 112210 (2021).
11. Van Cauwenberghe, L., Devriese, L., Galgani, F., Robbens, J. & Janssen, C. R. Microplastics in sediments: A review of techniques, occurrence and effects. *Mar. Environ. Res.* **111,** 5–17 (2015).
12. Hanvey, J. S. *et al.* A review of analytical techniques for quantifying microplastics in sediments. *Anal. Methods* **9,** 1369–1383 (2017).
13. Claessens, M., Van Cauwenberghe, L., Vandegehuchte, M. B. & Janssen, C. R. New techniques for the detection of microplastics in sediments and field collected organisms. *Mar. Pollut. Bull.* **70,** 227–233 (2013).
14. Samandra, S. *et al.* Quantifying environmental emissions of microplastics from urban rivers in Melbourne, Australia. *Mar. Pollut. Bull.* **189,** 114709 (2023).
15. Dikareva, N. & Simon, K. S. Microplastic pollution in streams spanning an urbanisation gradient. *Environ. Pollut.* **250,** 292–299 (2019).
16. Dikareva, N. & Simon, K. S. Factors Controlling Transport Dynamics of Microplastics in Streams. *ACS EST Water* **4,** 4120–4128 (2024).
17. Samandra, S. *et al.* Microplastic contamination of an unconfined groundwater aquifer in Victoria, Australia. *Sci. Total Environ.* **802,** 149727 (2022).
18. Truong, T. N. S. *et al.* Microplastic in atmospheric fallouts of a developing Southeast Asian megacity under tropical climate. *Chemosphere* **272,** 129874 (2021).
19. Zhang, Y. *et al.* Atmospheric microplastics: A review on current status and perspectives. *Earth-Sci. Rev.* **203,** 103118 (2020).
20. Padha, S., Kumar, R., Dhar, A. & Sharma, P. Microplastic pollution in mountain terrains and foothills: A review on source, extraction, and distribution of microplastics in remote areas. *Environ. Res.* **207,** 112232 (2022).
21. Ambrosini, R. *et al.* First evidence of microplastic contamination in the supraglacial debris of an alpine glacier. *Environ. Pollut.* **253,** 297–301 (2019).
22. Yang, Y. *et al.* Detection of Various Microplastics in Patients Undergoing Cardiac Surgery. *Environ. Sci. Technol.* **57,** 10911–10918 (2023).
23. Ragusa, A. *et al.* Plasticenta: First evidence of microplastics in human placenta. *Environ. Int.* **146,** 106274 (2021).
24. Horvatits, T. *et al.* Microplastics detected in cirrhotic liver tissue. *eBioMedicine* **82,** 104147 (2022).
25. Roslan, N. S. *et al.* Detection of microplastics in human tissues and organs: A scoping review. *J. Glob. Health* **14,** 04179 (2024).
26. Cverenkárová, K., Valachovičová, M., Mackul'ak, T., Žemlička, L. & Bírošová, L. Microplastics in the food chain. *Life* **11,** 1349 (2021).

27. Kwon, J. H. *et al.* Microplastics in food: A review on analytical methods and challenges. *Int. J. Environ. Res. Public Health* **17,** 6710 (2020).

28. Eerkes-Medrano, D., Leslie, H. A. & Quinn, B. Microplastics in drinking water: A review and assessment. *Curr. Opin. Environ. Sci. Health* **7,** 69–75 (2019).

29. Singh, S., Trushna, T., Kalyanasundaram, M., Tamhankar, A. J. & Diwan, V. Microplastics in drinking water: a macro issue. *Water Supply* **22,** 5650–5674 (2022).

30. Lau, W. W. Y. *et al.* Evaluating scenarios toward zero plastic pollution. *Science* **369,** 1455–1461 (2020).

31. Cai, H. *et al.* Analysis of environmental nanoplastics: Progress and challenges. *Chem. Eng. J.* **410,** 128208 (2021).

32. Zhu, L. *et al.* Transport of microplastics in the body and interaction with biological barriers, and controlling of microplastics pollution. *Ecotoxicol. Environ. Saf.* **255,** 114818 (2023).

33. Zhao, X. *et al.* Defining the size ranges of polystyrene nanoplastics according to their ability to cross biological barriers. *Environ. Sci. Nano* **10,** 2634–2645 (2023).

34. Prata, J. C., da Costa, J. P., Lopes, I., Duarte, A. C. & Rocha-Santos, T. Environmental exposure to microplastics: An overview on possible human health effects. *Sci. Total Environ.* **702,** 134455 (2020).

35. Pozo, K. *et al.* Persistent organic pollutants sorbed in plastic resin pellet - "Nurdles" from coastal areas of Central Chile. *Mar. Pollut. Bull.* **151,** 110786 (2020).

36. Symeonides, C. *et al.* An Umbrella Review of Meta-Analyses Evaluating Associations between Human Health and Exposure to Major Classes of Plastic-Associated Chemicals. *Ann. Glob. Health* **90,** 1–52 (2024).

37. da Costa, J. P., Santos, P. S., Duarte, A. C. & Rocha-Santos, T. (Nano)plastics in the environment - Sources, fates and effects. *Sci. Total Environ.* **566-567,** 15–26 (2016).

38. Liu, F., Zou, X., Yue, N., Zhang, W. & Zheng, W. Correlative Raman imaging and scanning electron microscopy for advanced functional materials characterization. *Cell Rep. Phys. Sci.* **4,** 101607 (2023).

39. Li, G. *et al.* Single-particle analysis of micro/nanoplastics by SEM-Raman technique. *Talanta* **249,** 123701 (2022).

40. Hernandez, L. M., Yousefi, N. & Tufenkji, N. Are There Nanoplastics in Your Personal Care Products? *Environ. Sci. Technol. Lett.* **4,** 280–285 (2017).

41. Piccardo, M., Renzi, M. & Terlizzi, A. Nanoplastics in the oceans: Theory, experimental evidence and real world. *Mar. Pollut. Bull.* **157,** 111317 (2020).

42. Parker, L. A. *et al.* Protocol for the production of micro and nanoplastic test materials. *Microplast. nanoplast.* **3,** 10 (2023).

43. Kooi, M. & Koelmans, A. A. Simplifying Microplastic via Continuous Probability Distributions for Size, Shape, and Density. *Environ. Sci. Technol. Lett.* **6,** 551–557 (2019).

44. Yesilkoy, F. *et al.* Ultrasensitive hyperspectral imaging and biodetection enabled by dielectric metasurfaces. *Nat. Photon.* **13,** 390–396 (2019).

45. Koshelev, K. *et al.* Subwavelength dielectric resonators for nonlinear nanophotonics. *Science* **367,** 288–292 (2020).

46. Kuznetsov, A. I., Miroshnichenko, A. E., Brongersma, M. L., Kivshar, Y. S. & Luk'yanchuk, B. Optically resonant dielectric nanostructures. *Science* **354,** aag2472 (2016).

47. Decker, M. & Staude, I. Resonant dielectric nanostructures: a low-loss platform for functional nanophotonics. *J. Opt.* **18,** 103001 (2016).

48. Krasnok, A., Caldarola, M., Bonod, N. & Alú, A. Spectroscopy and Biosensing with Optically Resonant Dielectric Nanostructures. *Adv. Opt. Mater.* **6,** 1701094 (2018).

49. Barreda, Á., Vitale, F., Minovich, A. E., Ronning, C. & Staude, I. Applications of Hybrid Metal-Dielectric Nanostructures: State of the Art. *Adv. Photon. Res.* **3,** 2100286 (2022).

50. West, J. L. & Halas, N. J. Engineered Nanomaterials for Biophotonics Applications: Improving Sensing, Imaging, and Therapeutics. *Annu. Rev. Biomed. Eng.* **5,** 285–292 (2003).

51. Lal, S., Link, S. & Halas, N. J. Nano-optics from sensing to waveguiding. *Nat. Photon.* **1,** 641–648 (2007).

52. Tittl, A., Giessen, H. & Liu, N. Plasmonic gas and chemical sensing. *Nanophotonics* **3,** 157–180 (2014).

53. Aigner, A. *et al.* Plasmonic bound states in the continuum to tailor light-matter coupling. *Sci. Adv.* **8,** eadd4816 (2022).

54. Kühner, L. *et al.* Radial bound states in the continuum for polarization-invariant nanophotonics. *Nat. Commun.* **13,** 4992 (2022).

55. Sadrieva, Z., Frizyuk, K., Petrov, M., Kivshar, Y. & Bogdanov, A. Multipolar origin of bound states in the continuum. *Phys. Rev. B* **100,** 115303 (2019).

56. Koshelev, K., Bogdanov, A. & Kivshar, Y. Meta-optics and bound states in the continuum. *Sci. Bull.* **64,** 836–842 (2019).

57. Hentschel, M. *et al.* Dielectric Mie voids: confining light in air. *Light Sci. Appl.* **12,** 3 (2023).

58. Caputo, F. *et al.* Measuring particle size distribution and mass concentration of nanoplastics and microplastics: addressing some analytical challenges in the sub-micron size range. *J. Colloid Interface Sci.* **588,** 401–417 (2021).

59. Molenaar, R. *et al.* Nanoplastic sizes and numbers: quantification by single particle tracking. *Environ. Sci.: Nano* **8,** 723–730 (2021).

60. Arslan, S. *et al.* Attoliter Mie Void Sensing. *arXiv,* 2407.02331 (2024).

61. Mintenig, S. M., Bäuerlein, P. S., Koelmans, A. A., Dekker, S. C. & Van Wezel, A. P. Closing the gap between small and smaller: towards a framework to analyse nano- and microplastics in aqueous environmental samples. *Environ. Sci. Nano* **5,** 1640–1649 (2018).

62. Floess, M. *et al.* 3D stimulated Raman spectral imaging of water dynamics associated with pectin-glycocalyceal entanglement. *Biomed. Opt. Express* **14,** 1460–1471 (2023).

63. Floess, M. *et al.* Limits of the detection of microplastics in fish tissue using stimulated Raman scattering microscopy. *Biomed. Opt. Express* **15,** 1528–1539 (2024).

64. Aspnes, D. E., Kelso, S. M., Logan, R. A. & Bhat, R. Optical properties of AlxGa1-x As. *J. Appl. Phys.* **60,** 754–767 (1986).

65. Sultanova, N., Kasarova, S. & Nikolov, I. Dispersion Properties of Optical Polymers. *APPA* **116,** 585–587 (2009).

66. Okoffo, E. D. & Thomas, K. V. Quantitative analysis of nanoplastics in environmental and potable waters by pyrolysis-gas chromatography–mass spectrometry. *J. Hazard. Mater.* **464,** 133013 (2024).

67. Rauert, C. *et al.* Assessing the Efficacy of Pyrolysis–Gas Chromatography–Mass Spectrometry for Nanoplastic and Microplastic Analysis in Human Blood. *Environ. Sci. Technol.* **59,** 1984–1994 (2025).

68. Workman, J. A Review of Spectroscopic Techniques used for the Quantification and Classification of Microplastics and Nanoplastics in the Environment. *Spectroscopy* (2024).